MAGNETIC RESONANCE
Open Access Discussions

1 # Heteronuclear and Homonuclear Radio Frequency Driven

2 # Recoupling

3 **Authors:** Evgeny Nimerovsky*, Kai Xue, Kumar Tekwani Movellan & Loren B. Andreas*

4 **Affiliations:**

5 Department of NMR based Structural Biology, Max Planck Institute for Biophysical Chemistry, Am

6 Fassberg 11, Göttingen, Germany

7 *Corresponding authors: land@nmr.mpibpc.mpg.de ORCID: 0000-0003-3216-9065 and

8 evni@nmr.mpibpc.mpg.de

9 **Abstract**

10 The Radio Frequency Driven Recoupling (RFDR) pulse sequence is used in magic-angle spinning

11 (MAS) NMR to recouple homonuclear dipolar interactions. Here we show simultaneous recoupling of both

12 the heteronuclear and homonuclear dipolar interactions by applying RFDR pulses on two channels. We

13 demonstrate the method, called HETeronuclear RFDR (HET-RFDR) on microcrystalline SH3 samples at

14 10 kHz and 55.555 kHz MAS. Numerical simulations of both HET-RFDR and standard RFDR sequences

15 allow better understanding of the influence of offsets, paths of magnetization transfers for both HET-RFDR

16 and RFDR experiments as well as the crucial role of XY phase cycling.

17 Keywords: Magic Angle Spinning NMR, heteronuclear and homonuclear RFDR, the operator analysis

18 **Introduction**

19 Magic-angle spinning (MAS) NMR spectroscopy is used to obtain atomic resolution spectra of

20 materials and biological molecules in the solid state, by removal of the broadening associated with

21 anisotropic dipolar couplings and other interactions. Under control of radio frequency pulses, dipolar

22   interactions can be switched on, or recoupled, in order to correlate nearby spins or to accurately determine

23   internuclear distances. Recoupling sequences can be broadly categorized as homonuclear (Bennett et al.,

24   1992; Ok et al., 1992; Zhang et al., 2020; Gelenter et al., 2020; Takegoshi et al., 2001; Szeverenyi et al.,

25   1982; Hou et al., 2011b, 2013; Carravetta et al., 2000; Bennett et al., 1998; Nielsen et al., 2012) or

26   heteronuclear (Gelenter et al., 2020; Gullion and Schaefer, 1989; Jaroniec et al., 2002; Hing et al., 1992;

27   Hartmann and Hahn, 1962; Rovnyak, 2008; Metz et al., 1994; Hediger et al., 1994; Hou et al., 2011a;

28   Brinkmann and Levitt, 2001; Gelenter and Hong, 2018; Zhang et al., 2016; Nielsen et al., 2012). The

29   homonuclear Radio Frequency Driven Recoupling (RFDR) sequence (Bennett et al., 1992) has been

30   successfully applied for the qualitative and quantitative determinations of the dipolar spin correlations in

31   materials (Saalwächter, 2013; Messinger et al., 2015; Fritz et al., 2019; Roos et al., 2018; Nishiyama et al.,

32   2014a; Wong et al., 2020; Hellwagner et al., 2018; Pandey and Nishiyama, 2018) and biomolecular samples

33   (Zheng et al., 2007; Tang et al., 2011; Shen et al., 2012; Pandey et al., 2014; Grohe et al., 2019; Andreas et

34   al., 2015; Petkova et al., 2002; Aucoin et al., 2009; Zinke et al., 2018; Zhang et al., 2017; Zhou et al., 2012;

35   Jain et al., 2017; Colvin et al., 2015; Shi et al., 2015; Daskalov et al., 2020). Sun et al. (1995) showed that

36   the RFDR pulse sequence element could also be used as a part of the SPICP experiment (Wu and Zilm,

37   1993) for removing the undesired effect of the chemical shift terms to zero order.

38   Depending on the assumptions (Ok et al., 1992; Ishii, 2001), two different Average Hamiltonian

39   Theory (Haeberlen and Waugh, 1968; Maricq, 1982) (AHT) descriptions have been detailed for RFDR. In

40   both, homonuclear dipolar recoupling occurs via a rotor-synchronized train of π-pulses, with one pulse each

41   rotor period (Bennett et al., 1992) on a single channel. In the first case, delta π-pulses are assumed (Bennett

42   et al., 1992). The efficiency of recoupling is linked with the rotational resonance conditions (Bennett et al.,

43   1992, 1998), and depends on the ratio between chemical shift offset difference and MAS rate. In the second

44   theoretical description, the effects of finite π-pulses are considered (Bennett et al., 1992; Ishii, 2001;

45   Nishiyama et al., 2014b; Zhang et al., 2015; Brinkmann et al., 2002; Ji et al., 2020). The efficiency of

46   recoupling in this case depends on a duty factor (Ishii, 2001), defined as the fraction of the rotor period

MAGNETIC RESONANCE
Open Access Discussions

47   occupied by the π-pulse. The RFDR pulses are applied according to a variety of xy phase cycling schemes,

48   which have been analyzed with the intent to suppress imperfections associated with offset differences, rf-

49   field inhomogeneity and second order Average Hamiltonian terms between different anisotropic

50   interactions (Zhang et al., 2015).

51   The full high field truncated dipolar Hamiltonian of the homonuclear I_2 spin system is represented

52   as follows:

53    $$H_{D,Full}^{II} = \omega_{D,12}(t)[3I_{z1}I_{z2} - \bar{I}_1 \cdot \bar{I}_2]. \quad \text{Eq. (1)}$$

54   where $\omega_{D,12}(t)$ is a periodic time dependent function (Olejniczak et al., 1984) that depends on the

55   positions of spins I_1 and I_2 within the rotor. This Hamiltonian is subsequently referred to as the full

56   Hamiltonian, and contains only the A and B terms of the dipolar alphabet (Slichter, 1990).

57   The interesting conclusion can be obtained, if we simplify the Eq. (1). The dipolar Hamiltonian

58   during RFDR can be simplified (in the absence of other interactions) by considering that $\bar{I}_1 \cdot \bar{I}_2$ commutes

59   with the secular part ($I_{z1}I_{z2}$) and with the rf-field Hamiltonian. At the end of each rotor period, the

60   oscillatory $\omega_{D,12}(t)$ term ensures zero total evolution. The simplified Eq. (1) is:

61    $$H_{D,M}^{II} = 1.5\omega_{D,12}(t)2I_{z1}I_{z2}. \quad \text{Eq. (2)}$$

62   Comparing Eq. (2) with full Dipolar Hamiltonian of the heteronuclear *IS* spin system(Mehring, 1983):

63    $$H_{D,Full}^{IS} = \omega_{D,12}(t)2I_zS_z, \quad \text{Eq. (3)}$$

64   we notice that the difference between Eq. (3) and Eq. (1) is a factor of 1.5. Note that we have made the

65   substitution of I_{z1} to I_z and I_{z2} to S_z while the dipolar function, $\omega_{D,12}(t)$, has been kept the same. Such

66   comparison suggests a HETeronuclear-RFDR (HET-RFDR), which should have a scaling of 1.5 as

67   compared with the homonuclear case.

68   In this article we investigate spin dynamics under HET-RFDR, in which RFDR π-pulses are

69   applied simultaneously on two channels (Figure 1). We demonstrate simultaneous heteronuclear and

70   homonuclear transfers using HET-RFDR applied to α-PET (Movellan et al., 2019) labeled SH3 at 10 kHz

71   and 55.555 kHz MAS.

72   We perform and compare a numerical operator analysis of both RFDR and HET-RFDR

73   experiments under different simulated conditions. This numerical analysis allows to define the conditions

74   under which homonuclear and heteronuclear RFDR polarization transfers have similar behaviors, to

75   understand the paths through which the signals are transferred between operators, and to understand the

76   crucial role of 90 degree phase alternation (XY-4, XY-8, etc) (Ishii, 2001; Nishiyama et al., 2014b; Zhang

77   et al., 2015; Hellwagner et al., 2018) for both RFDR and HET-RFDR recoupling.

78   **HET-RFDR Experiments**

79   Figure 1 shows two 2D (H)N(H)H pulse sequences used to evaluate the HET-RFDR transfer. For

80   both sequences, the transfer from proton to nitrogen is implemented with ramped cross polarization (CP)

81   and then the nitorgen dimension is encoded (t_1) for 2D spectra,).In Figure 1A, the transfer to structurally

82   interesting protons is implemented with N to H CP followed by H-H RFDR. In Figure 1B, the same

83   transfer is implemented with a single HET-RDFR period. The HET-RFDR transfer avoids the back CP

84   step. Instead, nitrogen polarization is placed along the $\hat{z}$ axis and transfered to directly bonded proton

85   spins and at the same time to remote proton spins with the simultaneous application of the π-pulses on the

86   proton and nitrogen channels.

87
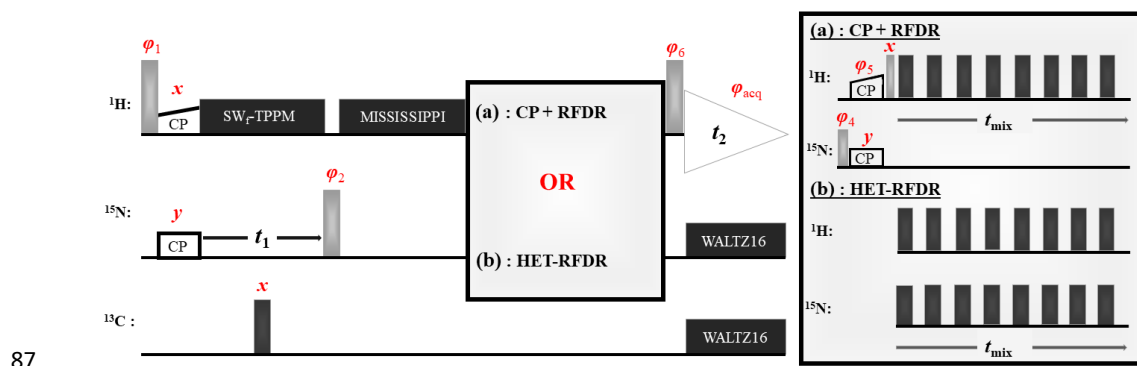
Figure 1 Two versions of the (H)N(H)H pulse sequence are shown. The first, (a), is the standard implementation with CP +

RFDR. The second, (b), instead uses the new HET-RFDR recoupling element. Light grey pulses represent $\pi/2$-pulses, whereas

dark grey pulses represent π-pulses. The ramped CP transfer from proton to nitrogen as well as from nitrogen to proton in (a) are

indicated with constant power on the nitrogen channel and a ramp in power on the proton chanenl. During the inderect dimension

(t_1), SW$_f$-TPPM decoupling is applied at 55 kHz , repectively. A single π-pulse in the middle of t_1 decouples carbon. Water

supression is implemented with the MISSISSIPI (Zhou and Rienstra, 2008) sequence. During acquisition, WALTZ16 (Thakur et

al., 2006) decoupling is applied on nitrogen and carbon channels. The phases are: $\varphi_1 = x, -x$; $\varphi_{acq} = y, -y, -y, y, -y, y, y, -y$.

In (a) the phases are: $\varphi_2 = x$; $\varphi_4 = x, x, -x, -x$; $\varphi_5 = y, y, y, y, -y, -y, -y, -y$; $\varphi_6 = x$. In (b) the phases are: $\varphi_2 =$

$x, x, -x, -x$; $\varphi_6 = x, x, x, x, -x, -x, -x, -x$. RFDR π-pulses on both channels use the XY8 scheme (Gullion et al., 1990).

Figure 2 compares the 1D and 2D spectra obtained with the two sequences of Figure 1. In Figure

2a, the 1D signal is shown as a function of RFDR mixing time. For the standard sequence (blue) the N to

H CP was 0.55 ms. The HET-RFDR signal is shown in (red). For the directly bonded amide protons, the

HET-RFDR polarization transfer achieves only ~40% of the CP signal. This occurs at 0.846 ms mixing

(second red spectrum). However, with increased mixing of about 3 ms, HET-RFDR reaches the same

efficiency as the standard sequence. This is notable since transfer over long distances has been

implemented with ~3 ms mixing for deuterated samples (Grohe et al., 2019; Linser et al., 2014).

Structurally interesting cross-peaks are indeed observed in the 2D HET-RFDR spectrum shown in

Figure 2b at both 1 ms (red) and 3 ms (cyan) mixing. For comparison, the (H)NH spectrum (without

RFDR mixing) is shown in black, to indicate the directly bonded amide correlations. For example, we

have observe the amide-amide contact between V44 and V53, which is 4.82 Å in the crystal (pdb code

5

108 2NUZ (Castellani et al., 2002)). The amide to side chain contact of a A55 N to Hβ (3.41 Å) is also

109 indicated in the Figure, along with a sequential contact from Y13 ^{15}N to L12 [1]Hα, which is 3.26 Å. These

110 peaks are boxed in Figure 2b, and the 1D slices shown above the 2D spectra. Comparing cross peak

111 intensities with the two mixing times, we observe an increase in signal for the longer 3 ms mixing,

112 indicating that the HET-RFDR sequence is indeed competitive for recording structurally interesting

113 contacts.
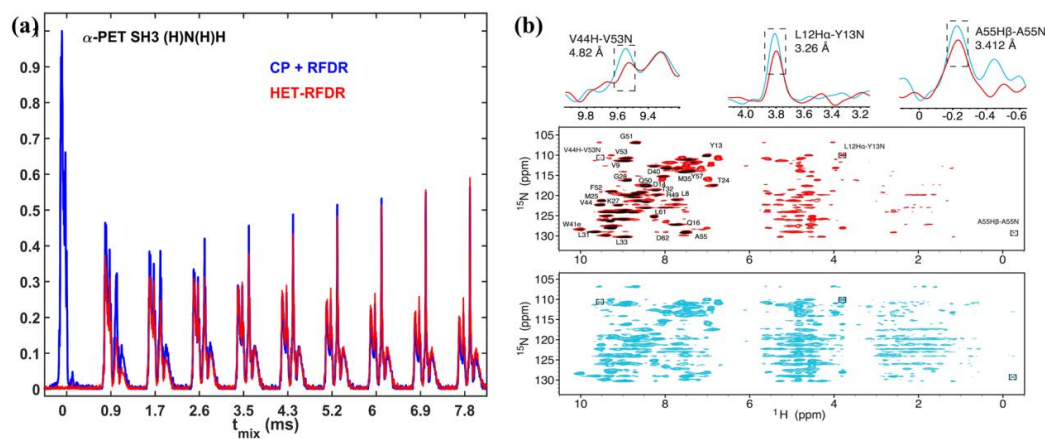
114

115 **Figure 2** 1D (a) and 2D (b) (H)N(H)H spectra of α-PET labeled SH3. For all spectra the first CP from proton to nitrogen was

116 performed with 1.05 ms. (a) 1D spectra with different sequences used for the second transfer: CP + RFDR (blue) and HET-RFDR

117 (red). For CP + RFDR, 0.55 ms of CP was used. For both RFDR and HET-RFDR, t_{mix} of 0, 0.846, 1.728, 2.592, 3.456, 4.32,

118 5.184, 6.048, 6.912, 7.7776 msare shown. (b) 2D HET-RFDR at two mixing times: 1.152 (red) and 3.456 (blue) ms. For

119 comparison, the CP based (H)N(H) spectrum is overlayed in black showing in-residue correlations. Spectra were recorded at a

120 600 MHz Bruker instrument equiped with a 1.3 mm probe and an MAS frequency of 55 kHz. The widths of π-pulses on proton

121 and nitrogen channels were 5.8 us and 6.6 us, respectively. The experimental parameters are detailed in Table 1 and 2 the

122 'Experimental Methods'.

123 At 55 kHz MAS on a 600 MHz instrument, the chemical shift offsets can always be much smaller

124 than the spinning frequency. At a lower MAS frequency, the offsets become important for HET-RFDR.

125 The recoupling then depends on a heteronuclear 'offset difference' that we define as $\Delta\Omega_{ij} = \Omega_i - \Omega_j$,

126 where Ω_i and Ω_j are the offsets on each channel (the difference between the Larmor frequency of the spin

127   and the carrier frequency (Bak et al., 2000)). The explanation of the following behavior is described in the

128   "Numerical Operator Analysis" section. When $\Omega_i = \Omega_j = 0$ as well as $\Delta\Omega_{ij} = \Omega_i - \Omega_j \approx n\nu_R$ (n=0, ±1,

129   ±2…), the HET-RFDR polarization transfer reaches local maximal intensities. However, when $\Delta\Omega_{ij} =$

130     $\Omega_i - \Omega_j \approx 0.5n\nu_R$ (n=±1, ±3…), the HET-RFDR polarization transfer reaches local minima. The

131   experimental confirmation of this is shown in Figure 3, where the effect of different proton and carbon

132   offsets is explored for proton-carbon HET-RFDR spectra. The spinning frequency was reduced to 10 kHz

133   MAS for these measurements and the signal detected on the carbon channel. The 1D HC HET-RFDR

134   pulse sequence is shown in the SI (Figure S1).

135   Figures 3a-e depicts the HET-RFDR spectra when the carbon carrier frequency is changed (numbers

136   show the offset from the alpha carbon at ~53 ppm), whereas the alpha proton offset is kept at 0 kHz (at

137   4.6 ppm). While heteronuclear transfer is detected at zero offset (Figure 3a) or with 11.1 kHz carbon

138   offset (Figure 3e), the signal remains in the noise when the carbon offset is 5.85 kHz (Figure 3c).

139   A similar effect can be detected when the proton carrier frequency is changed (increased from 4.6 ppm),

140   but this time the carbon offset is set to 5 kHz from Cα (83.66 ppm) to show that it is the offsets on both

141   channels ($\Delta\Omega_{C\alpha H\alpha}$) that is important (Figures 3f-j). The series of spectra show a local minimal transfers at

142   offset differences of 5 kHz (Figure 3f) and -5 kHz (Figure 3h) and local maximal polarization transfers at

143   differences of 0 (Figure 3g) and -10 kHz (Figure 3j).

144
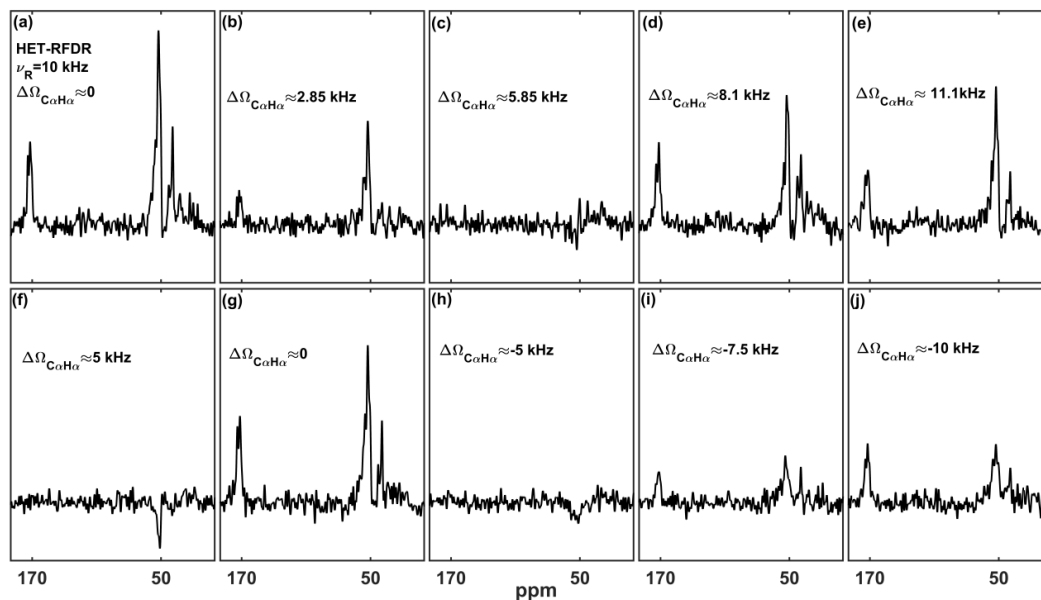
Figure 3 The influence of the carbon and proton offsets on proton-carbon HET-RFDR polarization transfers at 4.8 ms mixing.
α-PET labeled SH3 was used with 10 kHz MAS at a 600 MHz spectrometer using a 1.3 mm probe. The widths of π-pulses on proton and carbon channels were 5.8 us and 6.6 us, respectively. For (a)-(e) the proton carrirer frequency was set to 4.6 ppm and carbon carrier frequency was set to 51 ppm (a), 70 ppm (b), 90 ppm (c), 105 ppm (d) 125 ppm (e). For (f)-(j) the carbon carrirer frequency was set to 83.66 ppm and the proton carrier frequency was set to 4.6 ppm (f), 12.933 ppm (g), 21.26 ppm (h), 25.43 ppm (i) and 29.6 ppm (j). The indicated offset differences, $\Delta\Omega_{C\alpha H\alpha} = \Omega_{C\alpha} - \Omega_{H\alpha}$ in kHz were calculated based on typical isotropic chemical shifts of C_α (51 ppm) and H_α (4.6 ppm) at a 600 MHz spectrometer. The experimental parameters are detailed in Table 1 and 2 the 'Experimental Methods'. The 1D HET-RFDR sequence is shown in the SI (Figure S1).

Numerical Operator Analysis

To comprehend the mechanism underlying the transfers during the HET-RFDR and also the well-known RFDR pulse sequence, we use a numerical simulation approach. We identify the conditions under which the heteronuclear and homonuclear spin systems under HET-RFDR and RFDR sequences have similar behaviors. Considering the evolutions of the different spin systems through HET-RFDR and RFDR during the first two rotor periods, we identify the operators that are involved in the polarization transfer.

160   To identify the conditions under which the HET-RFDR and RFDR sequences have similar and

161   different behaviors we simulated a three spin system at high (55.555 kHz) and low (10 kHz) MAS

162   frequencies. In Figure 4 we compare the RFDR transferred signals for I_3 (a homonuclear 3-spin system,

163   black lines) and HET-RFDR transferred signals for *ISR* (three different types of spins with the names *I*, *S*

164   and *R*; red lines) spin systems. At 55.555 Hz MAS when the offset difference is small compared to MAS

165   rate, the behavior of the homonuclear I_3 spin system is similar to the behavior of the heteronuclear *ISR*

166   spin system (Figure 4a). However, when the MAS rate is low (10 kHz) and the offset difference cannot be

167   neglected, the behaviors of these spin systems are completely different (Figure 4b). For the homonuclear

168   spin system (I_3), the polarization transfers are efficient for all dipolar pairs (black lines), whereas for the

169   heteronuclear spin system (*ISR*) the HET-RFDR polarization transfer is detected between *R* and *I* spins

170   (Figure 4b, red dashed-dotted line) only. For this *RI* pair the offset difference was chosen as 10 kHz,

171   whereas for the other spin pairs (*SI*, *RS*) the offset differences were set to 5 kHz. These simulations show

172   a special condition of ∼$0.5\nu_R$ of offset difference for the heteronuclear spins under which the transfer is

173   negligible. The simulations are in full agreement with the experiments, which were shown in Figure 3.

174   Another interesting observation can be made from the influence of the offset difference on the RFDR

175   transfer for the homonuclear I_3 spin system (Figure 4b, black lines). For a 5 kHz of offset difference, the

176   RFDR polarization transfer between I_{z2} and I_{z3} spins is significantly faster with 10 kHz MAS (Figure 4b,

177   black dashed line) than at 55.555 kHz MAS (Figure 4a, black dashed line). Since the duty factor is

178   decreased with decreasing MAS frequency(Ishii, 2001): 0.33 for 55.555 kHz MAS and 0.06 for 10 kHz

179   MAS, the opposite behavior is expected if one considers only the effect of finite pulses in the RFDR

180   experiment(Ishii, 2001). It indicates that when the offset difference cannot be neglected with respect to

181   the MAS rate, it has a significant influence on the RFDR transfer efficiency between homonuclear spins

182   despite the significant remoteness from the rotational resonance condition (Bennett et al., 1992, 1998).
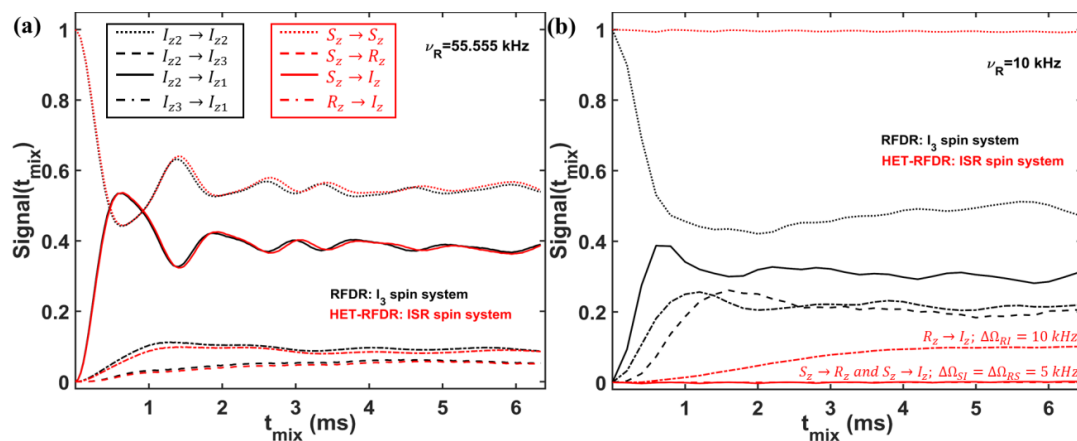
Figure 4 Comparison of the simulated RFDR and HET-RFDR signals. I_3 (three homonuclear spins, black lines) and *ISR* (three different spin types, red lines) for 55.555 kHz (a) and 10 kHz (b) MAS. 83 kHz of rf-field is used (6 us of the widths of π-pulses). The vertical axis shows the intensities of the starting and transferred signals between different operators of I_3 and *ISR* spin systems, respectively (the initial operator → the measured operator): $I_{z2} \rightarrow I_{z2}$ and $S_z \rightarrow S_z$ – (the dotted lines); $I_{z2} \rightarrow I_{z3}$ and $S_z \rightarrow R_z$ – (the dashed lines); $I_{z2} \rightarrow I_{z1}$ and $S_z \rightarrow I_z$ – (the solid lines); $I_{z3} \rightarrow I_{z1}$ and $R_z \rightarrow I_z$ – (the dashed-dotted lines). For both spin systems the offset (Ω) and CSA values are: [-3; 2; 7] (kHz) and [5.2; 2.5; 3].The dipolar coupling constants for homonuclear spin system (I_3) spin system are: $\nu_{12,D} = 7.333$ kHz, $\nu_{13,D} = 2$ kHz, $\nu_{23,D} = 0.333$ kHz. For *ISR* spin system all dipolar constants are 1.5 times larger: $\nu_{IS,D} = 11$ kHz, $\nu_{IR,D} = 3$ kHz, $\nu_{SR,D} = 0.5$ kHz. The simulated measurements occurs every 2 rotor periods. XY8 phase cycling is used. $I_{z1} \rightarrow I_{z1}, I_{z3} \rightarrow I_{z3}, I_z \rightarrow I_z$ and $R_z \rightarrow R_z$ are not shown.

In order to understand the different dependence on offset difference for the heteronuclear and homonuclear spin systems as well as via which operators the polarization transfer occurs, we considered the evolutions of two systems - I_2 homonuclear and *IS* heteronuclear spin systems - under RFDR and HET-RFDR sequences with 10 kHz MAS. We simulated the polarization transfers between different operators during the first two rotor periods, which completes the basic RFDR element: $t(\pi_x) \rightarrow del_1 \rightarrow t(\pi_y) \rightarrow del_2$. We consider the amplitudes of the operators for a single molecular orientation since it allows to see the significant evolution of the operators during the two rotor periods. Figure 5a,c,e shows the amplitudes of four Cartesian operators (Ernst et al., 1987) for *IS* (HET-RFDR) and Figures 5b,d,f

201   shows the operators for I_2 (RFDR) spin systems. The measured Cartesian operators are $I_z, S_z, 2I_xS_y, 2I_yS_x$

202   and $I_{z1}, I_{z2}, 2I_{x1}I_{y2}, 2I_{y1}I_{x2}$ for IS and I_2 spin systems, respectively.

203   The evolutions of four operators *during* two rotor periods for the IS spin system the I_2 spin system are

204   different, regardless of the offset difference. However, with a zero offset difference, the simulated

205   heteronuclear operators (Figure 5a) and the homonuclear operators (Figure 5b) show the same values of

206   the amplitudes at one and two rotor periods. From the 64 possibilites (details in the SI, section 'The

207   Operator Paths') for magnetization tranfer between heteronuclear operators I_z and S_z during the two rotor

208   periods, we find only one path with nonzero amplitude: $I_z \xrightarrow{\pi_x} 2I_xS_y \xrightarrow{del_1} 2I_xS_y \xrightarrow{\pi_y} S_z \xrightarrow{del_2} S_z$. In contrast to

209   the single path found for HET-RFDR, for the homonuclear case all 64 paths connecting operators I_{z1} and

210   I_{z2} have non-zero amplitudes. However, after each rotor period, the sum of all homonuclear paths provides

211   the same values of the amlitudes as for the heteronuclear IS spin system.

212   In contrast, with a non-zero offset difference, the amplitudes of homonuclear and heteronuclear operators

213   do not coinside at any time (Figures 5c and d). Moreover, while the amplitude of $I_{z1} \rightarrow I_{z2}$ polarization

214   transfer is sigificantly increased (Figure 5d, green line), the corresponding heteronuclear amplitude for

215    $I_z \rightarrow S_z$ transfer is sigificantly decreased (Figure 5c, green line).

216   In Figure 3 we experimentally demonstrated (it also was shown with simulations in Figure 4b), that when

217   the offset differences, $\Delta\Omega_{C\alpha H\alpha}$, were not neglected with respect to MAS rate, the minimal and maximal

218   HET-RFDR polarization transfers were achieved under $\pm\sim0.5\nu_R$ and $0, \pm\sim\nu_R$, respectively. Such

219   dependence on the offset difference for the heteronuclear spin system can be understood from Figure 5c,

220   where the simulations are performed with $0.5\nu_R$ offset difference. During the first π_x pulse the starting

221   signal is transferred from I_z to $2I_xS_y$. Because of the offset difference of $0.5\nu_R$, the amplitude of this

222   operator is mainly transferred to $2I_yS_x$ during the first delay (Figure 5c, red line). Since the second π-pulse

223   has phase y, there is no transfer from $2I_yS_x$ to I_{z2} and very little $I_z \rightarrow S_z$ polarization transfer overall by

224   the end of the second rotor period (Figure 5c, green line). Under $\pm\sim\nu_R$ offset difference the operator $2I_xS_y$

225   is transferred to itself during that first rotor period. Therefore the local maximal HET-RFDR polarization

226   transfer is detected. The sign, "~", is used since we consider the spin evolution with finite pulses.

227   Such dependence of the IS spin system on the offset difference indicates the importance of the

228   phase cycling for RFDR and HET-RFDR sequences. Figures 5d and f show the evolution of the operators

229   when there is no offset and both π-pulses have the same phase cycling – XX. For IS spin system (Figure

230   5e) only two operators have nonzero amplitudes during the investigated time: I_z (black line) and $2I_xS_y$

231   (blue line), whereas S_z and $2I_yS_x$ are not created. For the I_2 spin system (Figure 5d) all four operators

232   envolve during these two rotor periods. However, by the end of two rotor periods only two operators have

233   nonzero amplitudes, as for the IS spin system. In neither case is there magnetization transfer from I_z to S_z

234   nor from I_{z1} to I_{z2} after one or two rotor periods. The formal proof of zero transfer signal for homonuclear

235   two spin system in the absence of offset difference can be found in the SI, "RFDR Phase Cycling"

236   section.

237   Additional spectra and simulation results are found in the supporting information. We recorded

238   proton-carbon HET-RFDR spectra using fully protonated [^{13}C, ^{15}N] labeled SH3. We numerically

239   simulated multi-spin systems, either containing two protons and two carbons, or one nitrogen and two

240   protons, in order to track more complex transfer of magnetization. The main conclusions from the

241   simulations and the experiments in the SI are the agreement between experimental and simulated HET-

242   RFDR, and the expected small dependence of the HET-RFDR recoupling on the flip angle deviations

243   with XY8 phase cycling (Gullion et al., 1990).
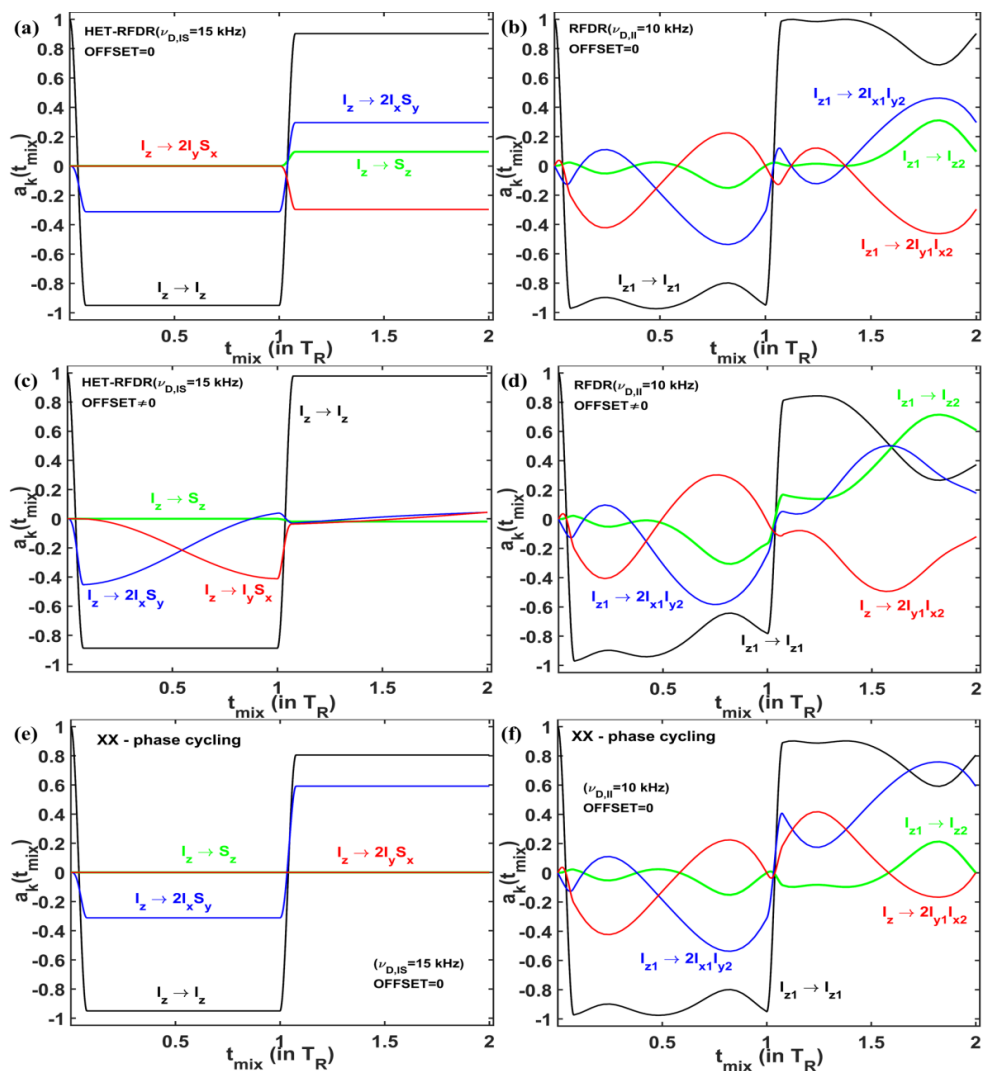
Figure 5 The operator evolution through HET-RFDR and RFDR over two rotor periods. The simulated amplitudes of the

operators of a single crystal (Euler angles: 184°; 141°; 349°) for HET-RFDR ((a), (c)) and RFDR ((b), (d)). For the heteronuclear

IS spin system, ($\nu_{D,IS} = 15$ kHz, the initial operator is I_z) and for the homonuclear I_2 spin system, ($\nu_{D,II} = 10$ kHz, the initial

operator is I_{z1}). The MAS frequency was 10 kHz and the rf-field was 65 kHz. Black lines – I_z and I_{z1}; Green lines – S_z and I_{z2};

Blue lines – $2I_xS_y$ and $2I_{x1}I_{y2}$; Red lines – $2I_yS_x$ and $2I_{y1}I_{x2}$. For (a) – (d) the phases of the first and second π-pulses are X and Y,

respectively. (e) and (f) show the case of IS and I_2 spin systems, respectively, when the phases of the first and second π-pulses are

both X. (a), (b), (e), (f) – Offset values in kHz: 0, 0. (c) and (d) – Offset values in kHz: 2, -3.

13

MAGNETIC RESONANCE
Open Access Discussions

Conclusion

252

253   In this article we firstly demonstrated HETeronuclear RFDR recoupling, when π-pulses with XY8

254   phase cycling were applied simultaneously on two channels. Observation of simultaneous heteronuclear

255   and homonuclear polarization transfers as well as long range contacts were observed in 2D (H)NH spectra

256   using HET-RFDR for the microcrystalline protein SH3 using α-PET labeling. The comparison of 1D

257   HET-RFDR with CP followed by homonuclear RFDR showed similar efficiency of both methods at long

258   mixing times of about 3ms and longer. We experimentally demonstrated and numerically explained the

259   dependence of the HET-RFDR efficiency on the offset difference between dipolar coupled spins. A

260   numerical operator analysis of both HET-RFDR and RFDR sequences showed that when the offest

261   difference was small with respect to the MAS frequency, and with measurement at a whole number of

262   rotor periods, the behavior of HET-RFDR was similar to the well-known homonuclear RFRD. However,

263   different behaviors were observed when the offset difference could not be neglected.

264   Considering the evoultion of a single crystal during HET-RFDR and RFDR, we showed the

265   operators that were responsible for the transfer. We demostrated that XY phase cycling of π-pulses has a

266   crucial role for both HET-RFDR and RFDR transfer. With phase cycling of XX (or $X\overline{X}$) the transfers

267   between heteronuclear and homonuclear spins did not occur in the absence of offsets. With the presence

268   of the offset differences when they cannot be neglected in comparison to the MAS rate, RFDR

269   polarization transfer with phase cycling of XX or $X\overline{X}$ does occur, although with lower efficiency as was

270   described before (Bennett et al., 1992).

271   **Experimental methods**

272   *Sample preparation*: Microcrystalline chicken alpha spectrin SH3 protein was used for acquisition of all

273   experimental data. The samples were labeled with 100% protonation at exchangeable sites and either with

274   alpha proton exchange by transamination (α-PET) or with uniform ^{13}C and ^{15}N labeling with the protocol

275   described in (Movellan et al., 2019).

MAGNETIC RESONANCE
Open Access Discussions

276   *Simulations*: HET-RFDR and RFDR simulations were performed with in-house MATLAB scripts using

277   numerical solution of the equation of motion (Nimerovsky and Goldbourt, 2012).

278   *Solid state NMR spectroscopy*: The HC and (H)N(H)H spectra of α-PET SH3 were acquired at 14.1 T (600

279   MHz) using a Bruker AVIIIHD spectrometer using a MASDVT600W2 BL1.3 HXY probe. The

280   experiments were performed at 10 kHz and 55.555 kHz MAS with the temperature of the cooling gas set

281   to 280 K and 235 K, respectively.

282   For 1D and 2D α-PET SH3 (H)N(H)H spectra, the ramped CP transfer from proton to nitrogen was

283   performed under the same conditions for all experiments: 42.95 kHz on the nitrogen channel and the optimal

284   ramped amplitude on the proton channel of 86.95-108.69 kHz. The mixing time was 1.05 ms. 9.3 kHz

285   WALTZ-16 (Shaka et al., 1983) with 25 us pulses and 10.4 kHz WALTZ-16 (Shaka et al., 1983) with 100

286   us pulses were applied on nitrogen and carbon channels during the acquisition. MISSISSIPPI water

287   suppression (Zhou and Rienstra, 2008) was applied for 100 ms with 13.513 kHz of the rf-field. The carrier

288   positions were set to 4.6 ppm, 118.5 ppm and 53.7 ppm for ^{1}H, ^{15}N and ^{13}C, respectively, except where

289   otherwise indicated.

290   Table 1 summarizes the applied experimental parameters for 1D spectra.

291   **Table 1** Summary of the experimental parameters used in the 1D CP + RFDR (the start and the end values are shown) and HET-

292   RFDR using α-PET labeled SH3.

	CP + RFDR		HET-RFDR
	CP	RFDR	
^{1}H (kHz)	86.95-108.69	86.21	86.21
^{15}N (kHz)	42.95	-	75.75
transfer time (ms)	0.55	[0-7.776]	[0-7.776]
NS	32		32
D1 (s)	2		2
AQ (s)	0.020448		0.020448
SW (kHz)	25		25

293   NS – number of scans; D1 – a recycle delay; AQ – the acquisition time; SW – the spectral width.

294 For 2D (H)N(H)H HET-RFDR spectra, during the indirect dimension 11.6 kHz SW_f-TPPM (Thakur et al.,

295 2006) decoupling with 36.36 us pulses was applied on the proton channel. Two mixing times were used:

296 1.152 ms and 3.456 ms. The widths of π-pulses on proton and nitrogen channels were 5.8 us and 6.6 us,

297 respectively. 16 scans were acquired per increment in t_1. The total time for the single 2D experiment was

298 10 hours. Table 2 summarizes the rest of the parameters.

299 **Table 2** Summary of the experimental parameters used in 2D HET HET-RFDR α-PET SH3 experiments.

	AQ1; AQ2 (s)	SW1; SW2 (kHz)	DW1; DW2 (us)
HET-RFDR	0.0527075; 0.020448	9.713; 25	102.94 20

300 1 and 2 are indirect and direct dimensions; AQ – the acquisition time; SW – the spectral width; DW – the dwell time.

301 For all 1D HC HET-RFDR experiments (Figure 3), 4.8 ms of the mixing time was applied. The widths of

302 π-pulses on proton and carbon channels were 5.8 us (86.21 kHz) and 6.6 us (75.75 kHz), respectively. 87

303 kHz SPINAL64 (Fung et al., 2000) with 6 us pulses was used during the acquisition. 128 scans were

304 accumulated. The spectral width was 50 kHz and the acquisition time 0.01536 s.

305 **Author Contributions**

306 EN performed the simulations and discovered heteronuclear HET-RFDR. EN and LBA designed

307 experiments. EN and KX recorded data. EN and LBA wrote the article. KTM prepared the SH3 protein

308 samples. All authors edited and approved the article.

309 **Competing Interests**

310 The authors declare that they have no conflict of interest.

311 **Acknowledgments**

314 **References**

315 Andreas, L. B., Le Marchand, T., Jaudzems, K., and Pintacuda, G.: High-resolution proton-detected NMR
316 of proteins at very fast MAS, J. Magn. Reson., 253, 36–49, https://doi.org/10.1016/j.jmr.2015.01.003,
317 2015.

318 Aucoin, D., Camenares, D., Zhao, X., Jung, J., Sato, T., and Smith, S. O.: High resolution 1H MAS RFDR
319 NMR of biological membranes, J. Magn. Reson. San Diego Calif 1997, 197, 77–86,
320 https://doi.org/10.1016/j.jmr.2008.12.009, 2009.

321 Bak, M., Rasmussen, J. T., and Nielsen, N. C.: SIMPSON : A General Simulation Program for Solid-State
322 NMR Spectroscopy, J. Magn. Reson. San Diego Calif 1997, 1–35,
323 https://doi.org/10.1006/jmre.2000.2179, 2000.

324 Bennett, A. E., Griffin, R. G., Ok, J. H., and Vega, S.: Chemical shift correlation spectroscopy in rotating
325 solids: Radio frequency-driven dipolar recoupling and longitudinal exchange, J. Chem. Phys., 96, 8624–
326 8627, https://doi.org/10.1063/1.462267, 1992.

327 Bennett, A. E., Rienstra, C. M., Griffiths, J. M., Zhen, W., Lansbury, P. T., and Griffin, R. G.: Homonuclear
328 radio frequency-driven recoupling in rotating solids, J. Chem. Phys., 108, 9463–9479,
329 https://doi.org/10.1063/1.476420, 1998.

330 Brinkmann, A. and Levitt, M. H.: Symmetry principles in the nuclear magnetic resonance of spinning
331 solids: Heteronuclear recoupling by generalized Hartmann–Hahn sequences, J. Chem. Phys., 115, 357–
332 384, https://doi.org/10.1063/1.1377031, 2001.

333 Brinkmann, A., Schmedt auf der Günne, J., and Levitt, M. H.: Homonuclear Zero-Quantum Recoupling in
334 Fast Magic-Angle Spinning Nuclear Magnetic Resonance, J. Magn. Reson., 156, 79–96,
335 https://doi.org/10.1006/jmre.2002.2525, 2002.

336 Carravetta, M., Edén, M., Zhao, X., Brinkmann, A., and Levitt, M. H.: Symmetry principles for the design
337 of radiofrequency pulse sequences in the nuclear magnetic resonance of rotating solids, Chem. Phys.
338 Lett., 321, 205–215, https://doi.org/10.1016/S0009-2614(00)00340-7, 2000.

339 Castellani, F., van Rossum, B., Diehl, A., Schubert, M., Rehbein, K., and Oschkinat, H.: Structure of a
340 protein determined by solid-state magic-angle-spinning NMR spectroscopy, Nature, 420, 99–102,
341 https://doi.org/10.1038/nature01070, 2002.

342 Colvin, M. T., Silvers, R., Frohm, B., Su, Y., Linse, S., and Griffin, R. G.: High Resolution Structural
343 Characterization of Aβ42 Amyloid Fibrils by Magic Angle Spinning NMR, J. Am. Chem. Soc., 137, 7509–
344 7518, https://doi.org/10.1021/jacs.5b03997, 2015.

345 Daskalov, A., Martinez, D., Coustou, V., Mammeri, N. E., Berbon, M., Andreas, L. B., Bardiaux, B., Stanek,
346 J., Noubhani, A., Kauffmann, B., Wall, J. S., Pintacuda, G., Saupe, S. J., Habenstein, B., and Loquet, A.:
347 Structural and molecular basis of cross-seeding barriers in amyloids, bioRxiv, 2020.07.06.188508,
348 https://doi.org/10.1101/2020.07.06.188508, 2020.

349 Ernst, R. R., Bodenhausen, G., and Wokaun, A.: Principles of nuclear magnetic resonance in one and two
350 dimensions, Oxford Univ. Press, London/New York, 610 pp., 1987.

351 Fritz, M., Kraus, J., Quinn, C. M., Yap, G. P. A., Struppe, J., Sergeyev, I. V., Gronenborn, A. M., and
352 Polenova, T.: Measurement of Accurate Interfluorine Distances in Crystalline Organic Solids: A High-
353 Frequency Magic Angle Spinning NMR Approach, J. Phys. Chem. B, 123, 10680–10690,
354 https://doi.org/10.1021/acs.jpcb.9b08919, 2019.

355 Fung, B. M., Khitrin, A. K., and Ermolaev, K.: An Improved Broadband Decoupling Sequence for Liquid
356 Crystals and Solids, J. Magn. Reson., 142, 97–101, https://doi.org/10.1006/jmre.1999.1896, 2000.

357 Gelenter, M. D. and Hong, M.: Efficient 15N–13C Polarization Transfer by Third-Spin-Assisted Pulsed
358 Cross-Polarization Magic-Angle-Spinning NMR for Protein Structure Determination, J. Phys. Chem. B,
359 122, 8367–8379, https://doi.org/10.1021/acs.jpcb.8b06400, 2018.

360 Gelenter, M. D., Dregni, A. J., and Hong, M.: Pulsed Third-Spin-Assisted Recoupling NMR for Obtaining
361 Long-Range 13C–13C and 15N–13C Distance Restraints, J. Phys. Chem. B, 124, 7138–7151,
362 https://doi.org/10.1021/acs.jpcb.0c04574, 2020.

363 Grohe, K., Nimerovsky, E., Singh, H., Vasa, S. K., Söldner, B., Voegeli, B., Rienstra, C. M., and Linser, R.:
364 Exact distance measurements for structure and dynamics in solid proteins by fast-magic-angle-spinning
365 NMR, Chem. Commun., https://doi.org/10.1039/C9CC02317H, 2019.

366 Gullion, T. and Schaefer, J.: Rotational-echo double-resonance NMR, J. Magn. Reson. 1969, 81, 196–200,
367 https://doi.org/10.1016/0022-2364(89)90280-1, 1989.

368 Gullion, T., Baker, D. B., and Conradi, M. S.: New, compensated Carr-Purcell sequences, J. Magn. Reson.
369 1969, 89, 479–484, https://doi.org/10.1016/0022-2364(90)90331-3, 1990.

370 Haeberlen, U. and Waugh, J. S.: Coherent Averaging Effect in Magnetic Resonance, Phys. Rev., 175, 453–
371 467, https://doi.org/10.1103/PhysRev.175.453, 1968.

372 Hartmann, S. R. and Hahn, E. L.: Nuclear Double Resonance in the Rotating Frame, Phys. Rev., 128,
373 2042–2053, https://doi.org/10.1103/PhysRev.128.2042, 1962.

374 Hediger, S., Meier, B. H., Kurur, N. D., Bodenhausen, G., and Ernst, R. R.: NMR cross polarization by
375 adiabatic passage through the Hartmann—Hahn condition (APHH), Chem. Phys. Lett., 223, 283–288,
376 https://doi.org/10.1016/0009-2614(94)00470-6, 1994.

377 Hellwagner, J., Wili, N., Ibáñez, L. F., Wittmann, J. J., Meier, B. H., and Ernst, M.: Transient effects in π-
378 pulse sequences in MAS solid-state NMR, J. Magn. Reson., 287, 65–73,
379 https://doi.org/10.1016/j.jmr.2017.12.015, 2018.

380 Hing, A. W., Vega, S., and Schaefer, J.: Transferred-echo double-resonance NMR, J. Magn. Reson. 1969,
381 96, 205–209, https://doi.org/10.1016/0022-2364(92)90305-Q, 1992.

382 Hou, G., Byeon, I.-J. L., Ahn, J., Gronenborn, A. M., and Polenova, T.: 1H–13C/1H–15N Heteronuclear
383 Dipolar Recoupling by R-Symmetry Sequences Under Fast Magic Angle Spinning for Dynamics Analysis of
384 Biological and Organic Solids, J. Am. Chem. Soc., 133, 18646–18655, https://doi.org/10.1021/ja203771a,
385 2011a.

386   Hou, G., Yan, S., Sun, S., Han, Y., Byeon, I.-J. L., Ahn, J., Concel, J., Samoson, A., Gronenborn, A. M., and
387   Polenova, T.: Spin Diffusion Driven by R-Symmetry Sequences: Applications to Homonuclear Correlation
388   Spectroscopy in MAS NMR of Biological and Organic Solids, J. Am. Chem. Soc., 133, 3943–3953,
389   https://doi.org/10.1021/ja108650x, 2011b.

390   Hou, G., Yan, S., Trébosc, J., Amoureux, J.-P., and Polenova, T.: Broadband homonuclear correlation
391   spectroscopy driven by combined R2nv sequences under fast magic angle spinning for NMR structural
392   analysis of organic and biological solids, J. Magn. Reson., 232, 18–30,
393   https://doi.org/10.1016/j.jmr.2013.04.009, 2013.

394   Ishii, Y.: 13C–13C dipolar recoupling under very fast magic angle spinning in solid-state nuclear magnetic
395   resonance: Applications to distance measurements, spectral assignments, and high-throughput
396   secondary-structure determination, J. Chem. Phys., 114, 8473–8483,
397   https://doi.org/10.1063/1.1359445, 2001.

398   Jain, M. G., Lalli, D., Stanek, J., Gowda, C., Prakash, S., Schwarzer, T. S., Schubeis, T., Castiglione, K.,
399   Andreas, L. B., Madhu, P. K., Pintacuda, G., and Agarwal, V.: Selective 1H–1H Distance Restraints in Fully
400   Protonated Proteins by Very Fast Magic-Angle Spinning Solid-State NMR, J. Phys. Chem. Lett., 8, 2399–
401   2405, https://doi.org/10.1021/acs.jpclett.7b00983, 2017.

402   Jaroniec, C. P., Filip, C., and Griffin, R. G.: 3D TEDOR NMR Experiments for the Simultaneous
403   Measurement of Multiple Carbon−Nitrogen Distances in Uniformly 13C,15N-Labeled Solids, J. Am.
404   Chem. Soc., 124, 10728–10742, https://doi.org/10.1021/ja026385y, 2002.

405   Ji, Y., Liang, L., Guo, C., Bao, X., Polenova, T., and Hou, G.: Zero-Quantum Homonuclear Recoupling
406   Symmetry Sequences in Solid-State Fast MAS NMR Spectroscopy, Acta Phys.-Chim. Sin., 36, 1905029–
407   1905034, 2020.

408   Linser, R., Bardiaux, B., Andreas, L. B., Hyberts, S. G., Morris, V. K., Pintacuda, G., Sunde, M., Kwan, A. H.,
409   and Wagner, G.: Solid-State NMR Structure Determination from Diagonal-Compensated, Sparsely
410   Nonuniform-Sampled 4D Proton–Proton Restraints, J. Am. Chem. Soc., 136, 11002–11010,
411   https://doi.org/10.1021/ja504603g, 2014.

412   Maricq, M. M.: Application of average hamiltonian theory to the NMR of solids, Phys. Rev. B, 25, 6622–
413   6632, https://doi.org/10.1103/PhysRevB.25.6622, 1982.

414   Mehring, M.: Principles of High Resolution NMR in Solids, 2nd ed., Springer-Verlag, Berlin Heidelberg,
415   https://doi.org/10.1007/978-3-642-68756-3, 1983.

416   Messinger, R. J., Ménétrier, M., Salager, E., Boulineau, A., Duttine, M., Carlier, D., Ateba Mba, J.-M.,
417   Croguennec, L., Masquelier, C., Massiot, D., and Deschamps, M.: Revealing Defects in Crystalline
418   Lithium-Ion Battery Electrodes by Solid-State NMR: Applications to LiVPO4F, Chem. Mater., 27, 5212–
419   5221, https://doi.org/10.1021/acs.chemmater.5b01234, 2015.

420   Metz, G., Wu, X. L., and Smith, S. O.: Ramped-Amplitude Cross Polarization in Magic-Angle-Spinning
421   NMR, J. Magn. Reson. A, 110, 219–227, https://doi.org/10.1006/jmra.1994.1208, 1994.

422   Movellan, K. T., Najbauer, E. E., Pratihar, S., Salvi, M., Giller, K., Becker, S., and Andreas, L. B.: Alpha
423   protons as NMR probes in deuterated proteins, J. Biomol. NMR, 73, 81–91,
424   https://doi.org/10.1007/s10858-019-00230-y, 2019.

425   Nielsen, N. Chr., Strassø, L. A., and Nielsen, A. B.: Dipolar Recoupling, in: Solid State NMR, edited by:
426   Chan, J. C. C., Springer, Berlin, Heidelberg, 1–45, https://doi.org/10.1007/128_2011_129, 2012.

427   Nimerovsky, E. and Goldbourt, A.: Insights into the spin dynamics of a large anisotropy spin subjected to
428   long-pulse irradiation under a modified REDOR experiment., J. Magn. Reson., 225, 130–41,
429   https://doi.org/10.1016/j.jmr.2012.09.015, 2012.

430   Nishiyama, Y., Malon, M., Ishii, Y., and Ramamoorthy, A.: 3D 15N/15N/1H chemical shift correlation
431   experiment utilizing an RFDR-based 1H/1H mixing period at 100kHz MAS, J. Magn. Reson., 244, 1–5,
432   https://doi.org/10.1016/j.jmr.2014.04.008, 2014a.

433   Nishiyama, Y., Zhang, R., and Ramamoorthy, A.: Finite-pulse radio frequency driven recoupling with
434   phase cycling for 2D 1H/1H correlation at ultrafast MAS frequencies, J. Magn. Reson., 243, 25–32,
435   https://doi.org/10.1016/j.jmr.2014.03.004, 2014b.

436   Ok, J. H., Spencer, R. G. S., Bennett, A. E., and Griffin, R. G.: Homonuclear correlation spectroscopy in
437   rotating solids, Chem. Phys. Lett., 197, 389–395, https://doi.org/10.1016/0009-2614(92)85790-H, 1992.

438   Olejniczak, E. T., Vega, S., and Griffin, R. G.: Multiple pulse NMR in rotating solids, J. Chem. Phys., 81,
439   4804–4817, https://doi.org/10.1063/1.447506, 1984.

440   Pandey, M. K. and Nishiyama, Y.: A one-dimensional solid-state NMR approach for 14NH/14NH overtone
441   correlation through 1H/1H mixing under fast MAS, Phys. Chem. Chem. Phys., 20, 25849–25853,
442   https://doi.org/10.1039/C8CP05000G, 2018.

443   Pandey, M. K., Vivekanandan, S., Yamamoto, K., Im, S., Waskell, L., and Ramamoorthy, A.: Proton-
444   detected 2D radio frequency driven recoupling solid-state NMR studies on micelle-associated
445   cytochrome-b5, J. Magn. Reson., 242, 169–179, https://doi.org/10.1016/j.jmr.2014.02.016, 2014.

446   Petkova, A. T., Ishii, Y., Balbach, J. J., Antzutkin, O. N., Leapman, R. D., Delaglio, F., and Tycko, R.: A
447   structural model for Alzheimer's -amyloid fibrils based on experimental constraints from solid state
448   NMR, Proc. Natl. Acad. Sci., 99, 16742–16747, https://doi.org/10.1073/pnas.262663499, 2002.

449   Roos, M., Mandala, V. S., and Hong, M.: Determination of Long-Range Distances by Fast Magic-Angle-
450   Spinning Radiofrequency-Driven 19F–19F Dipolar Recoupling NMR, J. Phys. Chem. B, 122, 9302–9313,
451   https://doi.org/10.1021/acs.jpcb.8b06878, 2018.

452   Rovnyak, D.: Tutorial on analytic theory for cross-polarization in solid state NMR, Concepts Magn. Reson.
453   Part A, 32A, 254–276, https://doi.org/10.1002/cmr.a.20115, 2008.

454   Saalwächter, K.: Robust NMR Approaches for the Determination of Homonuclear Dipole–Dipole
455   Coupling Constants in Studies of Solid Materials and Biomolecules, ChemPhysChem, 14, 3000–3014,
456   https://doi.org/10.1002/cphc.201300254, 2013.

457   Shaka, A. J., Keeler, J., Frenkiel, T., and Freeman, R.: An improved sequence for broadband decoupling:
458   WALTZ-16, J. Magn. Reson. 1969, 52, 335–338, https://doi.org/10.1016/0022-2364(83)90207-X, 1983.

459   Shen, M., Hu, B., Lafon, O., Trébosc, J., Chen, Q., and Amoureux, J.-P.: Broadband finite-pulse radio-
460   frequency-driven recoupling (fp-RFDR) with (XY8)41 super-cycling for homo-nuclear correlations in very
461   high magnetic fields at fast and ultra-fast MAS frequencies, J. Magn. Reson., 223, 107–119,
462   https://doi.org/10.1016/j.jmr.2012.07.013, 2012.

463   Shi, C., Fricke, P., Lin, L., Chevelkov, V., Wegstroth, M., Giller, K., Becker, S., Thanbichler, M., and Lange,
464   A.: Atomic-resolution structure of cytoskeletal bactofilin by solid-state NMR, Sci. Adv., 1,
465   https://doi.org/10.1126/sciadv.1501087, 2015.

466   Slichter, C. P.: Principles of Magnetic Resonance, 3rd ed., Springer-Verlag, Berlin Heidelberg,
467   https://doi.org/10.1007/978-3-662-09441-9, 1990.

468   Sun, B. Q., Costa, P. R., and Griffin, R. G.: Heteronuclear Polarization Transfer by Radiofrequency-Driven
469   Dipolar Recoupling Under Magic-Angle Spinning, J. Magn. Reson. A, 112, 191–198,
470   https://doi.org/10.1006/jmra.1995.1031, 1995.

471   Szeverenyi, N. M., Sullivan, M. J., and Maciel, G. E.: Observation of spin exchange by two-dimensional
472   fourier transform 13C cross polarization-magic-angle spinning, J. Magn. Reson. 1969, 47, 462–475,
473   https://doi.org/10.1016/0022-2364(82)90213-X, 1982.

474   Takegoshi, K., Nakamura, S., and Terao, T.: 13C–1H dipolar-assisted rotational resonance in magic-angle
475   spinning NMR, Chem. Phys. Lett., 344, 631–637, https://doi.org/10.1016/S0009-2614(01)00791-6, 2001.

476   Tang, M., Berthold, D. A., and Rienstra, C. M.: Solid-State NMR of a Large Membrane Protein by
477   Paramagnetic Relaxation Enhancement, J. Phys. Chem. Lett., 2, 1836–1841,
478   https://doi.org/10.1021/jz200768r, 2011.

479   Thakur, R. S., Kurur, N. D., and Madhu, P. K.: Swept-frequency two-pulse phase modulation for
480   heteronuclear dipolar decoupling in solid-state NMR, Chem. Phys. Lett., 426, 459–463,
481   https://doi.org/10.1016/j.cplett.2006.06.007, 2006.

482   Wong, K. M., Wang, Y., Seroski, D. T., Larkin, G. E., Mehta, A. K., Hudalla, G. A., Hall, C. K., and Paravastu,
483   A. K.: Molecular complementarity and structural heterogeneity within co-assembled peptide β-sheet
484   nanofibers, Nanoscale, 12, 4506–4518, https://doi.org/10.1039/C9NR08725G, 2020.

485   Wu, X. L. and Zilm, K. W.: Cross Polarization with High-Speed Magic-Angle Spinning, J. Magn. Reson. A,
486   104, 154–165, https://doi.org/10.1006/jmra.1993.1203, 1993.

487   Zhang, R., Nishiyama, Y., Sun, P., and Ramamoorthy, A.: Phase cycling schemes for finite-pulse-RFDR
488   MAS solid state NMR experiments, J. Magn. Reson., 252, 55–66,
489   https://doi.org/10.1016/j.jmr.2014.12.010, 2015.

490   Zhang, R., Mroue, K. H., and Ramamoorthy, A.: Proton-Based Ultrafast Magic Angle Spinning Solid-State
491   NMR Spectroscopy, Acc. Chem. Res., 50, 1105–1113, https://doi.org/10.1021/acs.accounts.7b00082,
492   2017.

493 Zhang, Z., Chen, Y., and Yang, J.: Band-selective heteronuclear dipolar recoupling with dual back-to-back
494 pulses in rotating solids, J. Magn. Reson., 272, 46–52, https://doi.org/10.1016/j.jmr.2016.09.003, 2016.

495 Zhang, Z., Oss, A., Org, M.-L., Samoson, A., Li, M., Tan, H., Su, Y., and Yang, J.: Selectively Enhanced 1H–
496 1H Correlations in Proton-Detected Solid-State NMR under Ultrafast MAS Conditions, J. Phys. Chem.
497 Lett., 11, 8077–8083, https://doi.org/10.1021/acs.jpclett.0c02412, 2020.

498 Zheng, Z., Qiang, W., and Weliky, D. P.: Investigation of finite-pulse radiofrequency-driven recoupling
499 methods for measurement of intercarbonyl distances in polycrystalline and membrane-associated HIV
500 fusion peptide samples, Magn. Reson. Chem., 45, S247–S260, https://doi.org/10.1002/mrc.2160, 2007.

501 Zhou, D. H. and Rienstra, C. M.: High-performance solvent suppression for proton detected solid-state
502 NMR, J. Magn. Reson., 192, 167–172, https://doi.org/10.1016/j.jmr.2008.01.012, 2008.

503 Zhou, D. H., Nieuwkoop, A. J., Berthold, D. A., Comellas, G., Sperling, L. J., Tang, M., Shah, G. J., Brea, E.
504 J., Lemkau, L. R., and Rienstra, C. M.: Solid-state NMR analysis of membrane proteins and protein
505 aggregates by proton detected spectroscopy, J. Biomol. NMR, 54, 291–305,
506 https://doi.org/10.1007/s10858-012-9672-z, 2012.

507 Zinke, M., Fricke, P., Lange, S., Zinn-Justin, S., and Lange, A.: Protein–Protein Interfaces Probed by
508 Methyl Labeling and Proton-Detected Solid-State NMR Spectroscopy, Chemphyschem, 19, 2457–2460,
509 https://doi.org/10.1002/cphc.201800542, 2018.

510

511